

CHARGED PARTICLE IDENTIFICATION WITH THE LIQUID XENON CALORIMETER OF THE CMD-3 DETECTOR

V.L. Ivanov^{a,b,1}, G.V. Fedotov^{a,b}, R.R. Akhmetshin^{a,b},
A.N. Amirkhanov^{a,b}, A.V. Anisenkov^{a,b}, V.M. Aulchenko^{a,b},
N.S. Bashtovoy^a, A.E. Bondar^{a,b}, A.V. Bragin^a, S.I. Eidelman^{a,b,c},
D.A. Epifanov^{a,b}, L.B. Epshteyn^{a,b,d}, A.L. Erofeev^{a,b},
S.E. Gayazov^{a,b}, A.A. Grebenuk^{a,b}, S.S. Gribanov^{a,b},
D.N. Grigoriev^{a,b,d}, F.V. Ignatov^{a,b}, S.V. Karpov^a,
V.F. Kazanin^{a,b}, A.A. Korobov^{a,b}, A.N. Kozyrev^{a,d},
E.A. Kozyrev^{a,b}, P.P. Krovovny^{a,b}, A.E. Kuzmenko^{a,b},
A.S. Kuzmin^{a,b}, I.B. Logashenko^{a,b}, P.A. Lukin^{a,b},
K.Yu. Mikhailov^a, V.S. Okhapkin^a, Yu.N. Pestov^a, A.S. Popov^{a,b},
G.P. Razuvaev^{a,b}, A.A. Ruban^a, N.M. Ryskulov^a,
A.E. Ryzhenenkov^{a,b}, A.V. Semenov^{a,b}, V.E. Shebalin^{a,b,e},
D.N. Shemyakin^{a,b}, B.A. Shwartz^{a,b}, E.P. Solodov^{a,b}, V.M. Titov^a,
A.A. Talyshev^{a,b}, S.S. Tolmachev^a, A.I. Vorobiov^a, Yu.V. Yudin^{a,b}

^a*Budker Institute of Nuclear Physics, SB RAS, Novosibirsk, 630090, Russia*

^b*Novosibirsk State University, Novosibirsk, 630090, Russia*

^c*Lebedev Physical Institute RAS, Moscow, 119333, Russia*

^d*Novosibirsk State Technical University, Novosibirsk, 630092, Russia*

^e*University of Hawaii, Honolulu, Hawaii 96822, USA*

Abstract

The paper describes a method of the charged particle identification, developed for the CMD-3 detector, installed at the VEPP-2000 e^+e^- collider. The method is based on the application of the boosted decision trees classifiers, trained for the optimal separation of electrons, muons, pions and kaons in the momentum range from 100 to 1200 MeV/ c . The input variables for

¹Corresponding author: V.L.Ivanov@inp.nsk.su

the classifiers are linear combinations of the energy depositions of charged particles in 12 layers of the liquid xenon calorimeter of the CMD-3. The event samples for training of the classifiers are taken from the simulation. Various issues of the detector response tuning in simulation and calibration of the calorimeter strip channels are considered. Application of the method is illustrated by the examples of separation of the $e^+e^-(\gamma)$ and $\pi^+\pi^-(\gamma)$ final states and of selection of the K^+K^- final state at high energies.

1. Introduction

The VEPP-2000 e^+e^- collider [1, 2, 3, 4] at the Budker Institute of Nuclear Physics (Novosibirsk, Russia) covers the center-of-mass (c.m.) energy ($E_{\text{c.m.}}$) range from 0.32 to 2.01 GeV and uses a technique of round beams to reach an instantaneous luminosity of $10^{32} \text{ cm}^{-2}\text{s}^{-1}$ at $E_{\text{c.m.}} = 2.0$ GeV. The Cryogenic Magnetic Detector (CMD-3) described in [5] is installed in one of the two interaction regions of the collider. The main goal of the CMD-3 is the precise measurement of the exclusive cross sections of e^+e^- annihilation into hadrons, which provides, for instance, a necessary input for the theoretical calculation of the hadronic contribution to the muon anomalous magnetic moment $(g - 2)_\mu$ and the running fine structure constant [6, 7, 8, 9].

The precise measurement of any hadronic cross section requires selection of a clean sample of signal events. The latter often requires the effective procedure of particle identification (PID), *i.e.* separation of electrons, muons, pions, kaons *etc.* In particular in the CMD-3:

- e^\pm identification can be performed on the base of the total energy deposition in the calorimeter [10];
- identification of muons can be carried out with the muon veto system;
- identification of antineutrons can be done with the time-of-flight system [11];

- separation of charged kaons and pions at the momenta less than 550 MeV/ c is performed using specific energy losses of particles in the drift chamber (dE/dx_{DC}) [12].

In this paper we describe a new technique of the charged PID based on the multiple measurements of the energy depositions of a particle in the layers of liquid xenon (LXe) calorimeter of the CMD-3 [13]. The LXe-based PID method is developed mainly for the task of K^\pm/π^\pm separation at momenta larger than 550 MeV/ c , where the dE/dx_{DC} -based PID is inefficient. For the hadronic final states like K^+K^- , $K^+K^-\pi^0$, $K^+K^-2\pi^0$, $K_S K^\pm \pi^\mp$ the LXe-based PID turns out to be an efficient tool for background suppression at high c.m. energies.

2. The liquid xenon calorimeter of the CMD-3 detector

The CMD-3 detector layout is shown in Fig. 1. The major tracking system is the cylindrical drift chamber (DC) [12], installed inside a thin ($0.085 X_0$) superconducting solenoid with 1.3 T magnetic field. Amplitude information from the DC signal wires is used to measure z -coordinates of tracks and ionization losses of charged particles. The endcap calorimeter is made of BGO crystals $13.4 X_0$ thick [10]. The barrel calorimeter consists of the inner LXe-based ($5.4 X_0$) ionization and outer CsI-based ($8.1 X_0$) scintillation calorimeters [14]. The total amount of material in front of the barrel calorimeter is $0.35X_0$.

The LXe calorimeter consists of a set of ionization chambers with seven cylindrical cathodes and eight anodes with a 10.2 mm gap between them, see Fig. 2. The electrodes are made of copper-plated G-10. The typical electric field in the gap is 1.1 kV/cm. The conductive surfaces of the anode electrodes are divided into rectangular pads, electrically connected by the wire going through the cathode layers. These 264 sets of pads form the towers oriented to the interaction point and are used to measure the energy deposition of the particles.

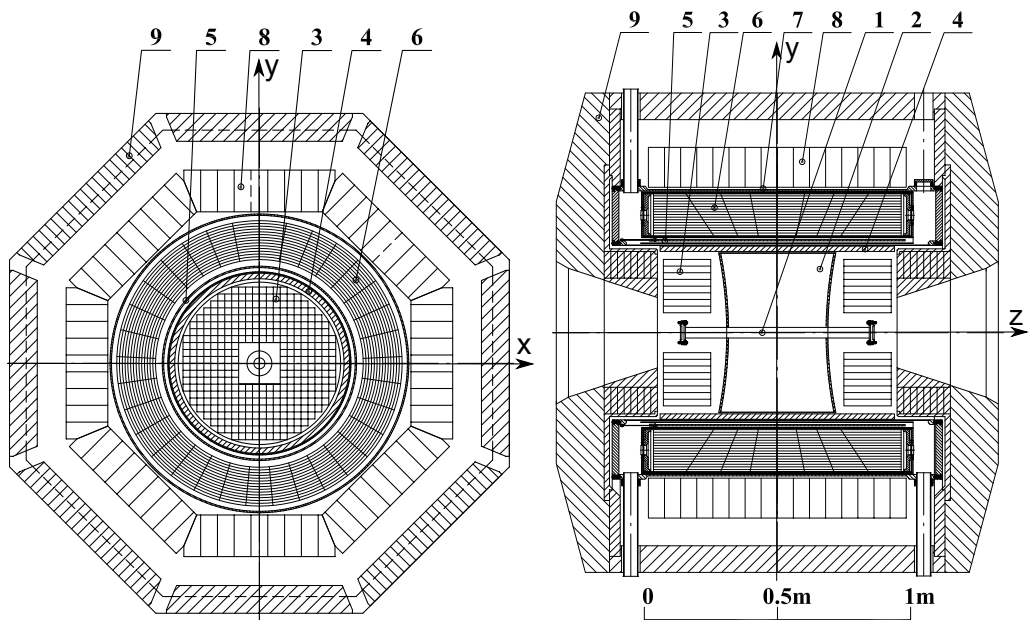


Figure 1: The CMD-3 detector layout: 1 — beam pipe, 2 — drift chamber, 3 — BGO end-cap calorimeter, 4 — Z-chamber (ZC), 5 — superconducting solenoid, 6 — LXe calorimeter, 7 — time-of-flight system (TOF), 8 — CsI calorimeter, 9 — yoke.

Both conductive surfaces of the cathode electrodes are divided into strips with a 1.2–1.8 mm width (depending on the layer), separated by the 1.5–2.0 mm gaps. A set of four consecutive strips is electrically connected to one superstrip making up one channel of electronics, see Fig. 3. The number of superstrips on one side of the cathode is 147–156. In what follows we refer to superstrips as just strips. The strips on the opposite sides of the cathode are mutually perpendicular that allows one to measure z and φ coordinates of the clusters.

A current induced on the strip during the ionization flow is integrated for $4.5 \mu\text{s}$, where the integration time corresponds to the maximum drift time of electrons in the gap. The strip channels are used for the measurements of the photon conversion point coordinates and the dE/dx of the particle in each of the 14 layers. Due to the gaps between the strips the cathodes are semitransparent, *i.e.* the ionization in one layer of the anode-cathode-anode double layer induces the charge on the strips of both sides of the cathode. This allows one to measure the coordinates of the point of photon conversion on the base of ionization that happened in one anode-cathode gap only.

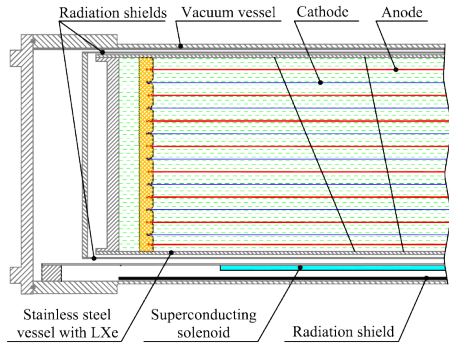


Figure 2: Structure of LXe calorimeter electrodes.

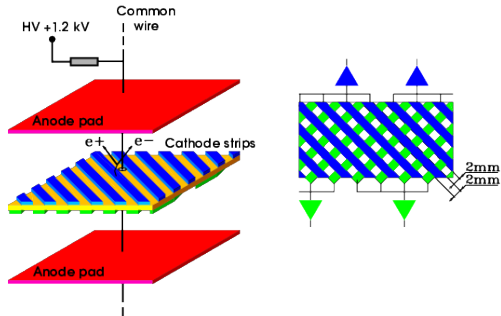


Figure 3: Anode-cathode-anode double layer of the LXe calorimeter and the strip structure of the cathode.

3. The idea of the PID procedure

In what follows we denote by dE/dx_{LXe} the energy deposition produced by a particle in each LXe layer, normalized to the *expected path length* d_{LXe} of the particle in the layer, estimated via the DC-track extrapolation. dE/dx_{LXe} is the single designation for the minimum ionizing and nuclear interacting particles as well as for the electromagnetic showers. The distributions of dE/dx_{LXe} in 14 LXe layers depending on the particle momentum for the simulated single e^\pm and μ^\pm , π^\pm and K^\pm are shown in Figs. 4 and 5, respectively. One should note the following features of dE/dx_{LXe} :

- In Figs. 4 and 5 a certain momentum threshold p_{thr} is seen for each particle type that corresponds to a minimum energy necessary to pass through the material in front of the LXe. Below this threshold only the products of the particle decay or nuclear interaction can reach the calorimeter. For kaons p_{thr}^K is about 300 MeV/c for the normal incident;
- The dE/dx_{LXe} spectra and the values of p_{thr} depend on d_{LXe} . This dependence is caused by the dependences of the shower development rate, the nuclear interaction probability, the particle deceleration rate *etc.* on d_{LXe} .

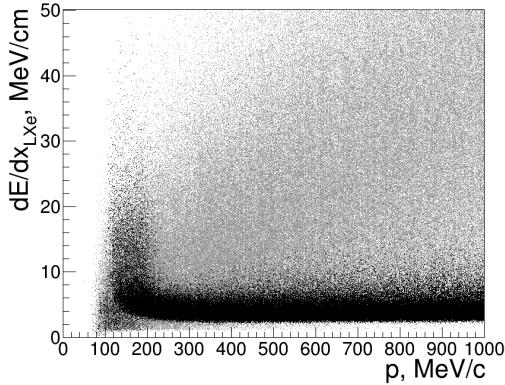


Figure 4: dE/dx_{LXe} in all LXe layers vs. particle momentum for e^\pm (gray) and μ^\pm (black) in simulation.

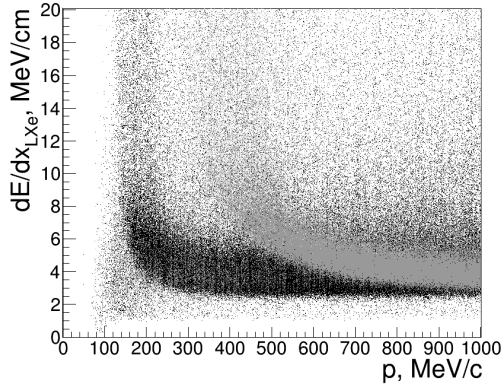


Figure 5: dE/dx_{LXe} in all LXe layers vs. particle momentum for K^\pm (gray) and π^\pm (black) in simulation.

The LXe-based PID method uses the difference in the dE/dx_{LXe} in the LXe-layers for different particle types. Namely, for each track in the DC reaching LXe, we calculate six values of the responses of the boosted decision trees (BDT) classifiers provided by the TMVA package [15], trained for optimal separation of particular pairs of particle types in certain ranges of the momentum p and d_{LXe} , *i.e.* in the $\Delta p_i \times \Delta d_{\text{LXe},j}$ cell. In what follows we denote these six values as $\text{BDT}(e^\pm, \mu^\pm)$, $\text{BDT}(e^\pm, \pi^\pm)$, $\text{BDT}(e^\pm, K^\pm)$, $\text{BDT}(\mu^\pm, \pi^\pm)$, $\text{BDT}(\mu^\pm, K^\pm)$, $\text{BDT}(\pi^\pm, K^\pm)$.

For training of each classifier we use samples of $\sim 10^5$ simulated events with single e^\pm , μ^\pm , π^\pm , K^\pm , having the momentum and d_{LXe} uniformly distributed in the $\Delta p_i \times \Delta d_{\text{LXe},j}$ cell. In total, we have 55 Δp_i cells of 20 MeV/ c width in the momentum range from 100 to 1200 MeV/ c and eight $\Delta d_{\text{LXe},j}$ cells (from 1.0 to 1.5 cm at large momenta). Thus, there is $2 \times 6 \times 55 \times 8 = 5280$ classifiers to be trained, where the factor of 2 stands for the two particle charges. The input variables for the classifiers are linear combinations of the dE/dx_{LXe} values in LXe layers described later in Section 5.

Since this PID method is based on the precise measurement of the energy deposition for different type of particles we need in the accurate energy calibration of the strip channels of the LXe calorimeter. Issues of the calibration of strip channels and the detector response tuning in MC are considered in the next sections.

4. Calibration of LXe calorimeter strip channels

In what follows we call *cluster* the group of the neighboring triggered strips (on one side of the cathode) with at least one strip having an amplitude above the *cluster reconstruction threshold*. This threshold is set to 1.5 MeV (in terms of the calibrated amplitude), which corresponds to the minimum amplitude induced by the minimum ionizing particles (MIPs) on the strip and is well above the level of electronics noise which energy equivalent is ~ 0.1 MeV. The cluster amplitude is equal to the sum of the amplitudes of its strips. The typical number of strips in the cluster for MIPs is 2–3.

The calibration of the strips is performed using events with cosmic muons having the momentum larger than 1 GeV/ c . There are three stages of the calibration:

1. Equalization of the strip amplitudes normalized to the particle path length, within each of seven cathodes separately;
2. Equalization of the cluster amplitudes normalized to the particle path length in all seven cathodes by bringing them to a common average;
3. Calculation of the MeV to ADC channel [16] transition coefficient.

The calibrated strip amplitude is calculated as $A_{\text{calib}} = A_{\text{raw}}K_3/(K_1K_2)$, where $K_{1...3}$ are the calibration coefficients of the corresponding stages, A_{raw} is the raw amplitude with the pedestal subtracted. To achieve the convergence of the $K_{1...3}$ the calibration is carried out iteratively: reconstruction of events at the current iteration is performed with the application of the calibration coefficients calculated at the previous iteration. To obtain the calibration precision of about 1%, three iterations are sufficient. The K_2 and K_3 are not calculated at the first iteration, since it does not make sense to clusterize non-equalized strips.

4.1. Equalization of the strip amplitudes within each cathode

The equalization of the strip amplitudes is performed by fitting the spectra of amplitudes of the *main* strips in the clusters, *i.e.* of the strips with the maximum amplitude, see Fig. 6. These amplitudes are normalized to the particle's path length to suppress the dependence on the inclination of the track in the anode-cathode gap. Let us denote by $A_{\text{main strip}}^{\text{max}}$ the position of the maximum of the normalized strip amplitude spectrum obtained from the Gaussian fit (Fig. 6). The K_1 for a given strip is calculated as the ratio

$$K_1 = A_{\text{main strip}}^{\text{max}} / \overline{A_{\text{main strip}}^{\text{max}}}, \quad (1)$$

where $\overline{A_{\text{main strip}}^{\text{max}}}$ is the average maximum position for the strips on both sides of the given cathode.

Simulation of cosmic muons reveals the residual angular dependence of the $K_{1,MC}$ manifested as the systematic $\pm 1\%$ modulation of the $K_{1,MC}$ for different strips, see Fig. 7. The same modulation is seen in the difference between the K_1 coefficients, calculated in the experiment on the base of events with cosmic muons ($K_{1,cosmic}$) and using muons from the process $e^+e^- \rightarrow \mu^+\mu^-$ ($K_{1,\mu^+\mu^-}$). Since muons from the process $e^+e^- \rightarrow \mu^+\mu^-$ have the uniform azimuthal angle distribution, there is no azimuthal modulation in $K_{1,\mu^+\mu^-}$. To account for observed modulation the experimental K_1 is multiplied by the approximated angular dependence of the $K_{1,MC}$ (Fig. 7).

Figure 8 shows the K_1 trends for the first and second calibration iterations in the runs of 2020 year.

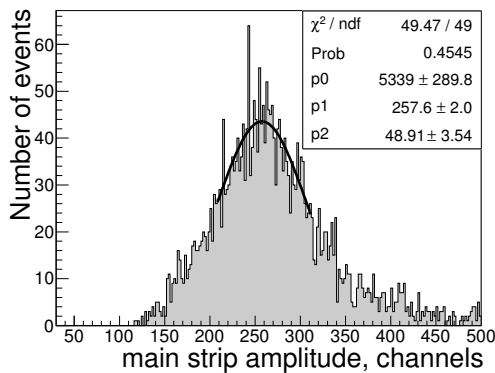


Figure 6: Typical amplitude spectrum of the strip cluster main strip and its Gaussian approximation near the maximum. The amplitude is normalized to the particle path length.

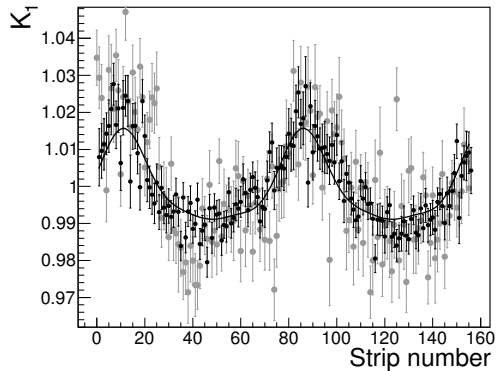


Figure 7: $K_{1,MC}$ dependence on the strip number for simulated cosmic muons (black markers) and its approximation (black curve). The $K_{1,cosmic} - K_{1,\mu^+\mu^-}$ difference in the experiment as a function of the strip number is shown by the gray markers.

4.2. Equalization of average cluster amplitudes between cathodes

At the second stage we equalize the average cluster amplitudes normalized to the particle's path length, $\overline{dE/dx}_{clust}^l$, $l = 1..7$, between cathodes. The average is calculated near the maximum of spectra in the limits containing $\sim 90\%$ of events. The calibration coefficients K_2^l bringing the $\overline{dE/dx}_{clust}^l$ on each cathode to the common interlayer average are calculated as

$$K_2^l = \frac{\overline{dE/dx}_{\text{clust}}^l}{\sum_{l=1}^7 \overline{dE/dx}_{\text{clust}}^l / 7}. \quad (2)$$

The same equalization procedure is performed for simulation. Figure 9 shows the K_2^l trends for different cathodes at the second calibration iteration in the 2020 runs.

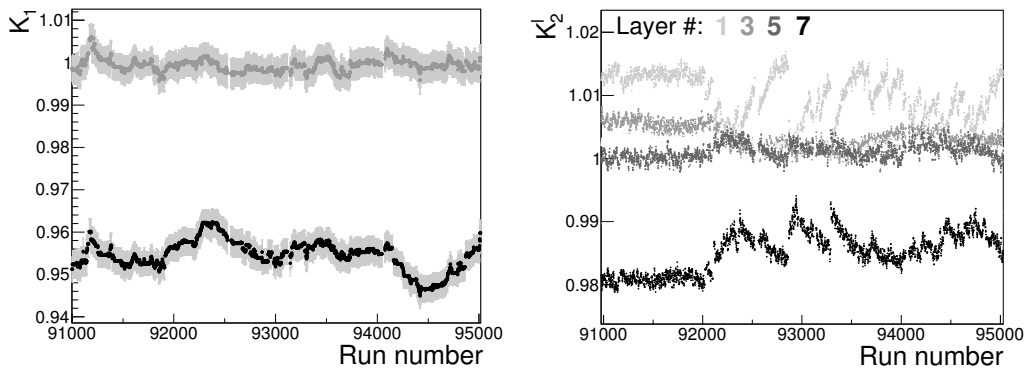


Figure 8: The typical K_1 trend for one strip at the first (black) and second (gray) calibration iterations in the 2020 runs. The gray bands show the statistical uncertainties. Figure 9: The K_2^l trends for different cathodes at the second calibration iteration in the 2020 runs, see color/double layer correspondence in the legend.

4.3. Calculation of the MeV/channel transition coefficient

We calculate the MeV/channel transition coefficient K_3 via the relation

$$K_3 = \frac{\sum_{l=1}^7 \overline{dE/dx}_{\text{clust}}^{l,\text{MC}}}{\sum_{l=1}^7 \overline{dE/dx}_{\text{clust}}^{l,\text{data}}} \cdot K_{3,\text{MC}}[\text{MeV/channel}], \quad (3)$$

where $K_{3,\text{MC}}$ is the transition coefficient tabulated in the MC. Figure 10 shows the K_3 trends for the second and third calibration iterations in the 2020 runs.

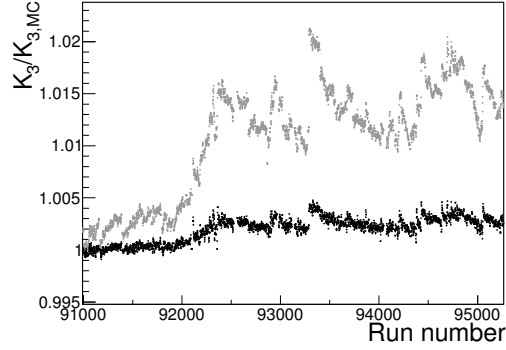


Figure 10: The $K_3/K_{3,\text{MC}}$ trends at the second (gray) and third (black) calibration iterations in the 2020 runs.

5. Detector response tuning in simulation

5.1. Tuning for minimum ionizing particles

Figure 11 shows dE/dx_{LXe} of the cosmic muons measured in the innermost double layer by the upper strips (dE/dx_{up}) vs. that measured by the lower strips (dE/dx_{low}). The events in the pair of inclined bands correspond to the cases, when the large ionization in one anode-cathode gap induces the large amplitude on the strips on the opposite side due to the cathode transparency. This cross-layer induction, compared with the normal interlayer induction, occurs with some suppression factor, which depends on the position of the ionization in the gap. The average of this factor over all possible ionization positions is called the *transparency coefficient* T_l , $l = 1 \dots 7$. The T_l depends on the geometry of the cathode, namely on the widths of the strips and the gaps and on the thickness of dielectric. Initially we fix the T_l values to the *a priori* value of 0.17 for all double layers.

The transparency mixes up the real energy depositions $dE/dx_{\text{low, up}}^{\text{real}}$ into the amplitudes measured by the lower and upper strips $dE/dx_{\text{low, up}}^{\text{meas}}$:

$$\begin{bmatrix} dE/dx_{\text{up}}^{\text{meas}} \\ dE/dx_{\text{low}}^{\text{meas}} \end{bmatrix} = \frac{1}{1 + T_l} \begin{bmatrix} 1 & T_l \\ T_l & 1 \end{bmatrix} \cdot \begin{bmatrix} dE/dx_{\text{up}}^{\text{real}} \\ dE/dx_{\text{low}}^{\text{real}} \end{bmatrix}. \quad (4)$$

These relations should be understood as correct on average, or as the definitions of $dE/dx_{\text{low, up}}^{\text{real}}$. For convenience in what follows we operate with the half sum and the half difference of the $dE/dx_{\text{low, up}}^{\text{real}}$:

$$\begin{bmatrix} dE/dx_{\text{summ}} \\ dE/dx_{\text{diff}} \end{bmatrix} = \frac{1}{2(1 - T_l)} \begin{bmatrix} 1 & 1 \\ 1 & -1 \end{bmatrix} \cdot \begin{bmatrix} 1 & -T_l \\ -T_l & 1 \end{bmatrix} \cdot \begin{bmatrix} dE/dx_{\text{up}}^{\text{meas}} \\ dE/dx_{\text{low}}^{\text{meas}} \end{bmatrix}. \quad (5)$$

We use dE/dx_{summ} and dE/dx_{diff} in six inner double layers as the input variables of the BDT classifiers, described in Section 3. The outer seventh double layer suffers from the incomplete xenon fill and is not used in PID. The data/MC comparison of the dE/dx_{summ} spectra for cosmic muons reveals the relative broadening of the experimental spectra, see Fig. 12 (in what follows the simulated histograms are normalized to the number of events in the experimental one unless otherwise stated). The alleged reason of the broadening is the complicated cathode structure, not taken into account in the MC, where the cathode is supposed to be just a solid plane. To account for this broadening, we add in simulation the random Gaussian noise to the amplitudes induced on the strips on both sides of the cathode. The width of the Gaussian noise is taken the same for all double layers, its energy equivalent is ~ 0.8 MeV. The resulting simulation agrees well with the data, see Fig. 12.

Next, Fig. 13 shows the distribution of the dE/dx_{diff} vs. dE/dx_{summ} for the cosmic muons in the innermost double layer in the experiment. The vertical lines show the slices of the distribution, inside which we perform the data/MC comparison of the dE/dx_{diff} spectra. For example, such a comparison for the third double layer is shown in Fig. 14. Since the position of the peaks in Fig. 14 is mainly controlled by the T_l , the discrepancy between the data/MC peak positions means that the *a priori* taken T_l values are wrong. We tune the T_l values to achieve the coincidence of the peaks and thus obtain the true transparency coefficients $T_1 = 0.23$, $T_2 = 0.22$, $T_3 = 0.35$, $T_4 = 0.32$, $T_5 = 0.35$, $T_6 = 0.33$, $T_7 = 0.33$ with about 5% uncertainty.

Apart from the shift of the peak positions we observe the relative broadening of the experimental dE/dx_{diff} spectra, presumably related to the vari-

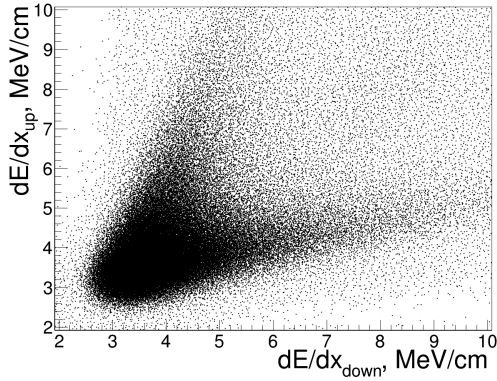


Figure 11: dE/dx_{LXe} for cosmic muons measured in the innermost double layer by the upper strips vs. that measured by the lower strips in the experiment.

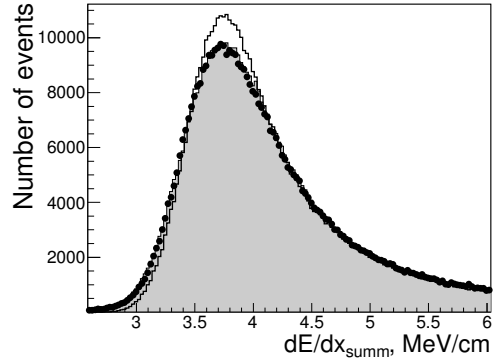


Figure 12: The dE/dx_{summ} spectra in the innermost double layer for cosmic muons in the experiment (markers) and MC before (open histogram) and after (gray histogram) tuning.

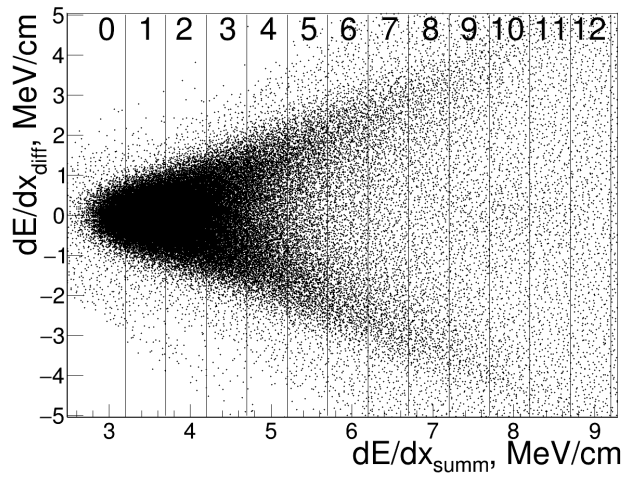


Figure 13: The dE/dx_{diff} vs. dE/dx_{summ} distribution for the cosmic muons in the innermost double layer in the experiment. The slicing on the dE/dx_{summ} is also shown.

ation of the transparency around its average value of T_l . To account for this broadening, we add the anticorrelated Gaussian noise to the amplitudes, induced on the upper and lower strips in simulation. This means that the same random value is added to the amplitude of the upper strips and subtracted from the amplitude of the lower strips. This additional anticorrelated noise simulates the effect of the redistribution of the charge between upper and lower strips due to the T_l variations. The variance of the additional noise is tuned individually in all double layers, the noise energy equivalents are $\sim 0.6 - 0.12$ MeV depending on the layer. After the applied corrections we observe a good data/MC agreement in the dE/dx_{diff} spectra, see Fig. 14.

5.2. Tuning for electromagnetic shower

Another kind of the data/MC discrepancy is observed in the dE/dx_{summ} spectra for the electromagnetic (e.m.) showers, produced in the calorimeter by electrons and positrons from the process $e^+e^- \rightarrow e^+e^-$, see Fig. 15. The additional noises used for tuning of the MIPs in simulation show no serious effect on the large amplitudes of the e.m. showers. The actual reasons of the observed discrepancy remain unclear, but many possible sources were studied, including the imprecise description of the dead material in front of the calorimeter, the influence of the electronegative admixtures in LXe, the inaccurate value of LXe density *etc.* Fortunately, the discrepancy can be mostly eliminated by the simple linear transformation of the simulated amplitudes $dE/dx^{\text{meas, corr}} = a \cdot dE/dx^{\text{meas}} - b$, where $a = 1.055$ is the “additional calibration” coefficient for the showers and $b = 0.7$ is the shift introduced to reach the data/MC coincidence of the minimum ionizing peaks in the innermost double layer. The resulting data/MC good agreement (except the innermost double layer), shown in Fig. 15, is conserved for all e^\pm momenta and angles.

6. Spectra of classifier response and signal/background separation power

In this section we perform the data/MC comparison of the resulting BDT response spectra for different types of particles. Figures 16–21 provide a

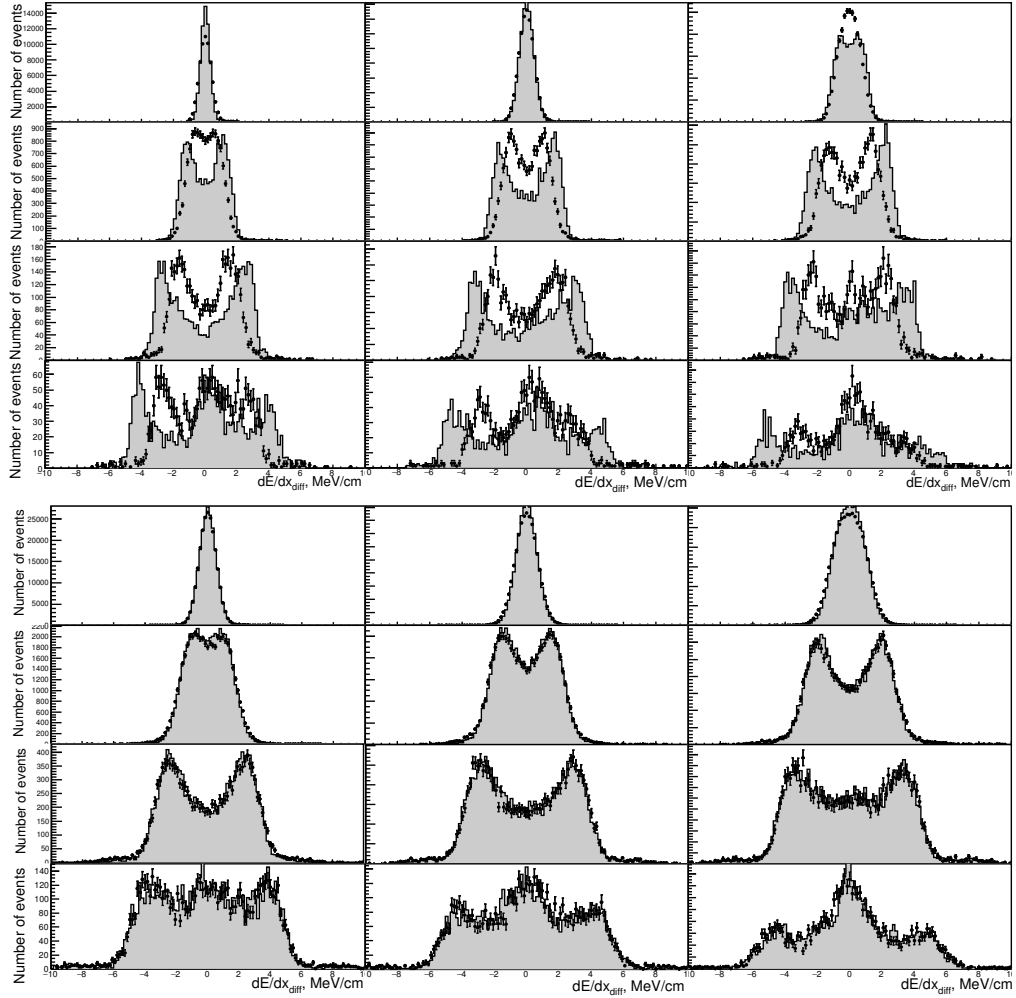


Figure 14: The dE/dx_{diff} spectra for the cosmic muons in the third double layer in all slices in the experiment (markers) and MC (gray histogram) before (upper figure) and after (lower figure) T_1 tuning and addition of the anticorrelated noise.

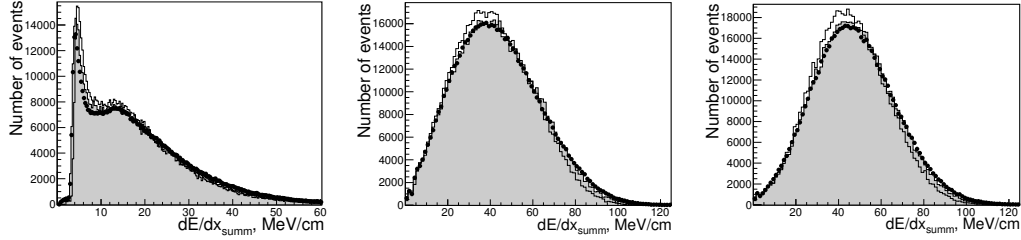


Figure 15: The dE/dx_{summ} spectra in the first (left), third (middle) and fifth (right) double layers for e^\pm from the process $e^+e^- \rightarrow e^+e^-$ in the experiment (markers), MC before (open histogram) and after (gray histogram) linear transformation. The beam energy is 987.5 MeV.

general view of the potential effectiveness of all six types of classifiers as a function of particle momentum according to simulation. The “comb” in the BDT spectra at low momentum corresponds to the cases when all input variables of the classifiers are zero. It is seen, that μ/π separation (Fig. 19) is not effective at all, whereas separation of e^\pm from μ^\pm , π^\pm and K^\pm (Figs. 16–18) is effective starting from some threshold momentum.

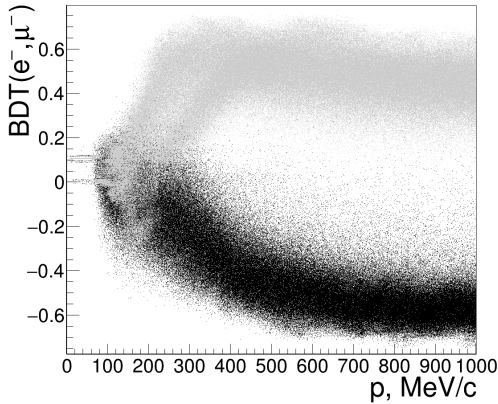


Figure 16: The $\text{BDT}(e^-, \mu^-)$ vs. particle momentum for simulated e^- (black) and μ^- (gray), uniformly distributed in d_{LXe} .

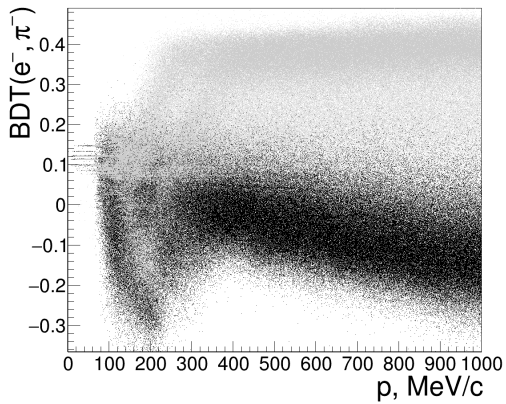


Figure 17: The $\text{BDT}(e^-, \pi^-)$ vs. particle momentum for simulated e^- (black) and π^- (gray), uniformly distributed in d_{LXe} .

6.1. Electrons/positrons

We select e^\pm from $e^+e^- \rightarrow e^+e^-$ events using the following criteria: 1) there are exactly two DC-tracks with the opposite charges; 2) the $|\rho|$ and $|z|$ of the

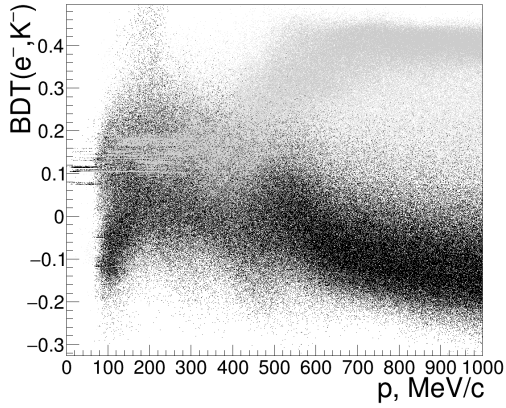


Figure 18: The $BDT(e^-, K^-)$ vs. particle momentum for the simulated e^- (black) and K^- (gray), uniformly distributed in d_{LXe} .

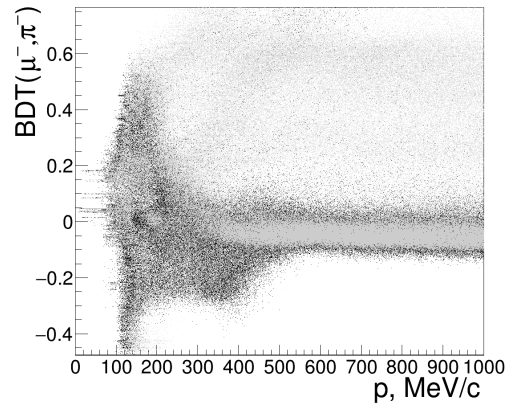


Figure 19: The $BDT(\mu^-, \pi^-)$ vs. particle momentum for simulated μ^- (black) and π^- (gray), uniformly distributed in d_{LXe} .

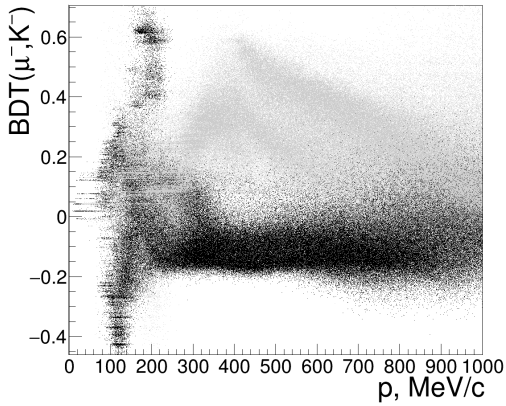


Figure 20: The $BDT(\mu^-, K^-)$ vs. particle momentum for simulated μ^- (black) and K^- (gray), uniformly distributed in d_{LXe} .

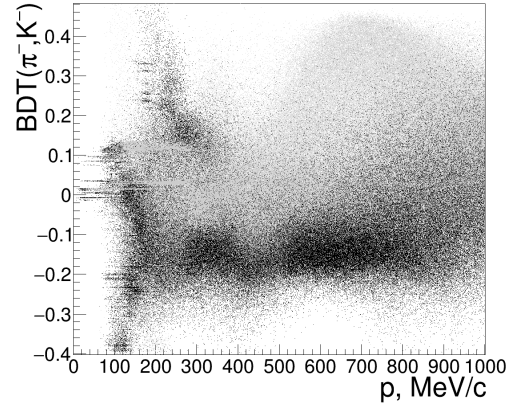


Figure 21: The $BDT(\pi^-, K^-)$ vs. particle momentum for simulated π^- (black) and K^- (gray), uniformly distributed in d_{LXe} .

track point of the closest approach to the beam axis should be less than 0.6 and 12 cm, respectively; 3) the polar angles of tracks should be in the range from 0.9 to $\pi - 0.9$ rad; 4) the tracks are collinear: $|\theta_1 + \theta_2 - \pi| < 0.15$ rad and $||\varphi_1 - \varphi_2| - \pi| < 0.15$ rad; 5) the energy deposition of each particle in the barrel calorimeter (LXe and CsI) is larger than the half beam energy (E_{beam}). Data/MC comparison for the $\text{BDT}(e^\pm, \mu^\pm)$, $\text{BDT}(e^\pm, \pi^\pm)$ and $\text{BDT}(e^\pm, K^\pm)$ spectra for the selected e^\pm at the low (280 MeV) and high (987.5 MeV) beam energies is shown in Fig. 22. Agreement is good in all cases.

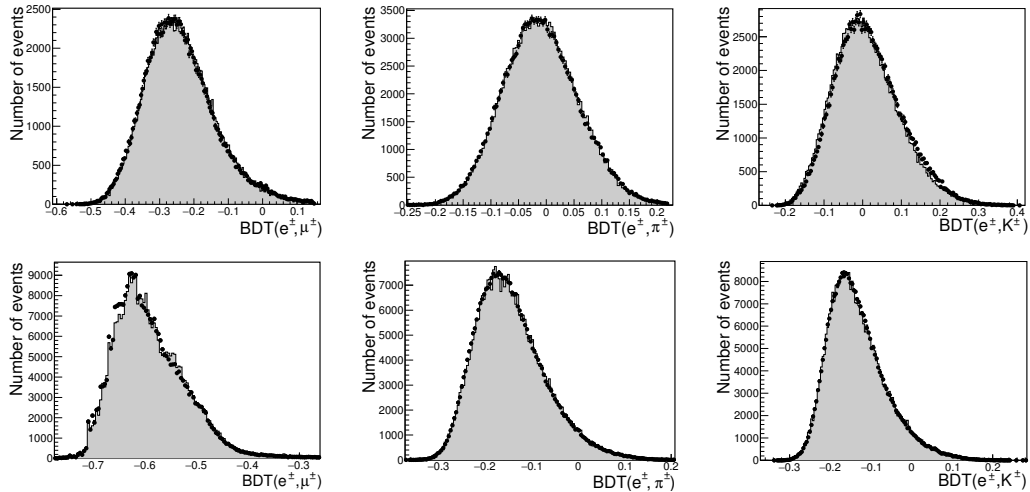


Figure 22: The $\text{BDT}(e^\pm, \mu^\pm)$ (left), $\text{BDT}(e^\pm, \pi^\pm)$ (middle) and $\text{BDT}(e^\pm, K^\pm)$ (right) spectra for the e^\pm selected from $e^+e^- \rightarrow e^+e^-$ events in the experiment (markers) and MC (gray histogram) at $E_{\text{beam}} = 280$ MeV (top figures) and $E_{\text{beam}} = 987.5$ MeV (bottom figures).

6.2. Muons

We select a sample of μ^\pm from events with cosmic muons using the following criteria: 1) there is only one DC-track; 2) the track momentum is in the range from 100 to 1200 MeV/ c ; 3) track is not central: the minimal distance from the track to the beam axis is in the range from 3 to 15 cm; 4) the energy deposition of the particle in the calorimeter is less than 400 MeV. Reasonable data/MC agreement for the $\text{BDT}(e^\pm, \mu^\pm)$, $\text{BDT}(\mu^\pm, \pi^\pm)$ and $\text{BDT}(\mu^\pm, K^\pm)$ spectra can be seen in Fig. 23.

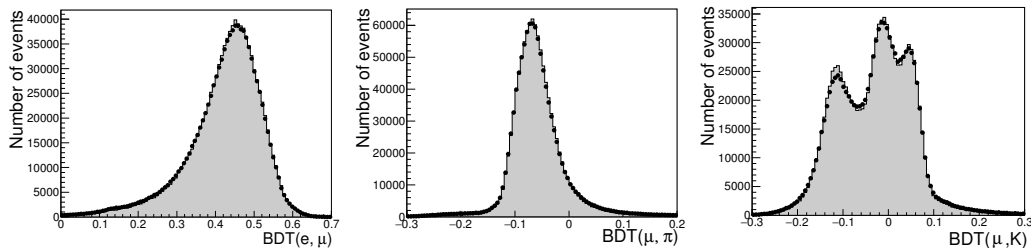


Figure 23: The $\text{BDT}(e^\pm, \mu^\pm)$ (left), $\text{BDT}(\mu^\pm, \pi^\pm)$ (middle) and $\text{BDT}(\mu^\pm, K^\pm)$ (right) spectra for the cosmic μ^\pm in the experiment (markers) and MC (gray histogram). The muon momentum is in the range from 100 to 1200 MeV/c.

6.3. Pions

The clean π^\pm sample with well-predicted angular-momentum distributions can be obtained by selection of $e^+e^- \rightarrow \phi(1020) \rightarrow \pi^+\pi^-\pi^0$ events. To do this, we search for events with exactly two DC-tracks with opposite charges and momenta larger than 100 MeV/c. Then, there should be not less than two photons with energies larger than 40 MeV. Sorting over all the pairs of such photons, we perform the 4C-kinematic fit for two tracks and the photon pair assuming energy-momentum conservation and choose the pair giving the smallest χ_{4C}^2 . If the invariant mass of the photon pair $m_{2\gamma}$ satisfies the $|m_{2\gamma} - m_{\pi^0}| < 40 \text{ MeV}/c^2$ condition, we consider the $\pi^+\pi^-\pi^0$ event as reconstructed.

First of all, since simulation of nuclear interactions of pions is not perfect, we check the data/MC agreement in the dE/dx_{summm} and dE/dx_{diff} spectra for selected π^\pm , see Fig. 24. The agreement is good for all pion momenta. Then, Fig. 25 shows good data/MC agreement for the $\text{BDT}(e^\pm, \pi^\pm)$, $\text{BDT}(\mu^\pm, \pi^\pm)$ and $\text{BDT}(\pi^\pm, K^\pm)$ spectra. The agreement is good for both pion charges. The efficiency of e^- rejection vs. the efficiency of π^- selection (ROC-curve) for the $\text{BDT}(e^-, \pi^-)$ at different pion momenta is shown in Fig. 26.

6.4. Kaons

The clean K^\pm sample can be selected from the four-track $e^+e^- \rightarrow K^+K^-\pi^+\pi^-$ events. We select these events on the base of $\sim 60 \text{ pb}^{-1}$ of integrated luminosity collected in the 2019 runs and use data from all energy points above

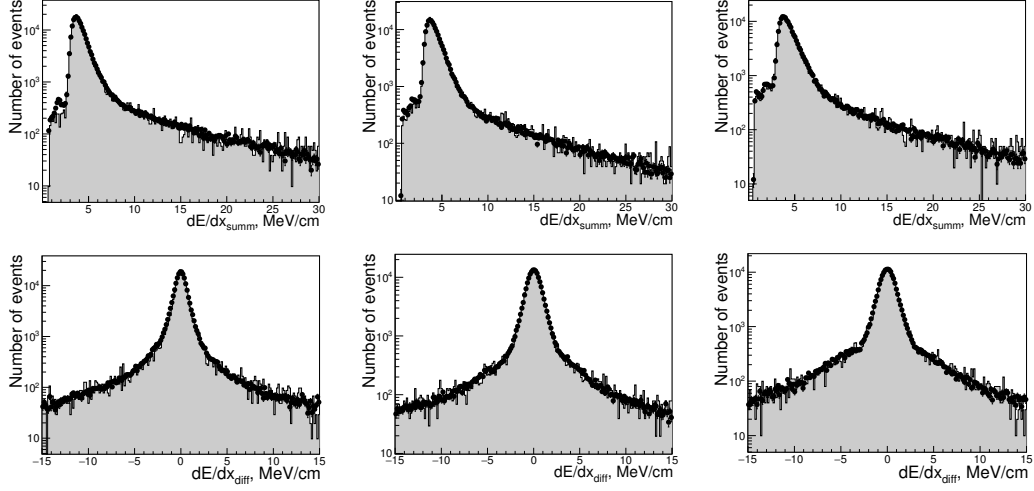


Figure 24: The dE/dx_{summ} (top figures) and dE/dx_{diff} (bottom figures) in the 1st (left), 3rd (middle) and 5th (right) double layers for the π^\pm selected from $e^+e^- \rightarrow \pi^+\pi^-\pi^0$ events in the experiment (markers) and simulation (gray histogram). The c.m. energy is 1019 MeV ($\phi(1020)$ meson peak).

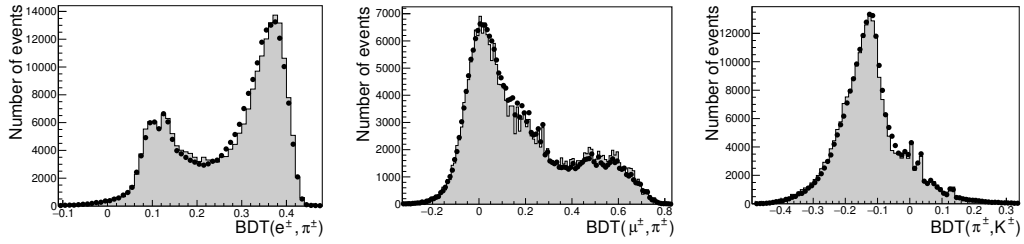


Figure 25: The $\text{BDT}(e^\pm, \pi^\pm)$ (left), $\text{BDT}(\mu^\pm, \pi^\pm)$ (middle) and $\text{BDT}(\pi^\pm, K^\pm)$ (right) spectra for the π^\pm selected from $e^+e^- \rightarrow \pi^+\pi^-\pi^0$ events in the experiment (markers) and MC (gray histogram). The c.m. energy is 1019 MeV ($\phi(1020)$ meson peak).

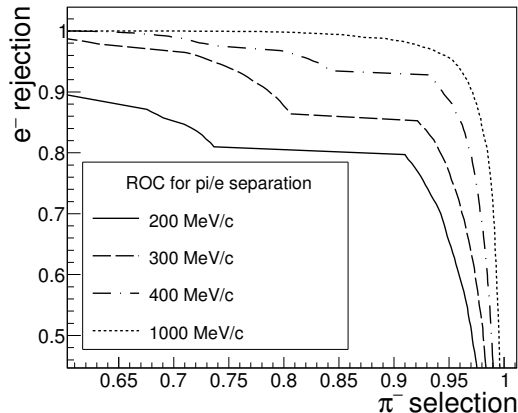


Figure 26: The ROC-curves for the $\text{BDT}(e^-, \pi^-)$ classifier for different particle momenta (see legend) according to simulation.

the reaction threshold. The event selection procedure involves the kinematic energy-momentum selections along with the cuts on the value of the likelihood function, based on the dE/dx_{DC} of tracks, as described in [17, 18]. However, a large part of selected kaons has the momenta lower than the $p_{\text{trh}}^{\text{K}} \sim 300 \text{ MeV}/c$, and for such momenta only the products of kaon decay or nuclear interaction can reach the LXe.

Similarly to the case of pions, we check the accuracy of simulation of the nuclear interactions of kaons by the data/MC comparison for the dE/dx_{summ} and dE/dx_{diff} spectra for selected K^\pm , see Fig. 27. The agreement is reasonable for all kaon momenta. The data/MC comparison for the $\text{BDT}(e^\pm, K^\pm)$, $\text{BDT}(\mu^\pm, K^\pm)$ and $\text{BDT}(\pi^\pm, K^\pm)$ spectra is shown in Fig. 28. The simulated $\text{BDT}(\pi^\pm, K^\pm)$ spectrum seems somewhat distorted for K^\pm with low momenta (lower left picture in Fig. 28), presumably due to the inaccuracy in the simulation of nuclear interactions. However, the distortion mostly disappears at large kaon momenta, see lower right picture in Fig. 28.

The LXe-based π/K separation is of special importance in the studies of the hadronic processes with K^\pm , and it should be compared with the separation based on dE/dx_{DC} . Figure 29 shows the distributions of the dE/dx_{DC} vs. momentum for the simulated K^\pm and π^\pm . The ROC-curves

for both types of classification at different particle momenta are shown in Fig. 30. At the momenta below 400 MeV/c the LXe-based classifier has poor efficiency. At the largest momenta its efficiency gradually reduces due to the decrease of the difference between kaon and pion ionization losses, see Fig. 5. However, the LXe-based π/K separation remains effective at the momenta 650–900 MeV/c, where the dE/dx_{DC} -based separation does not work.

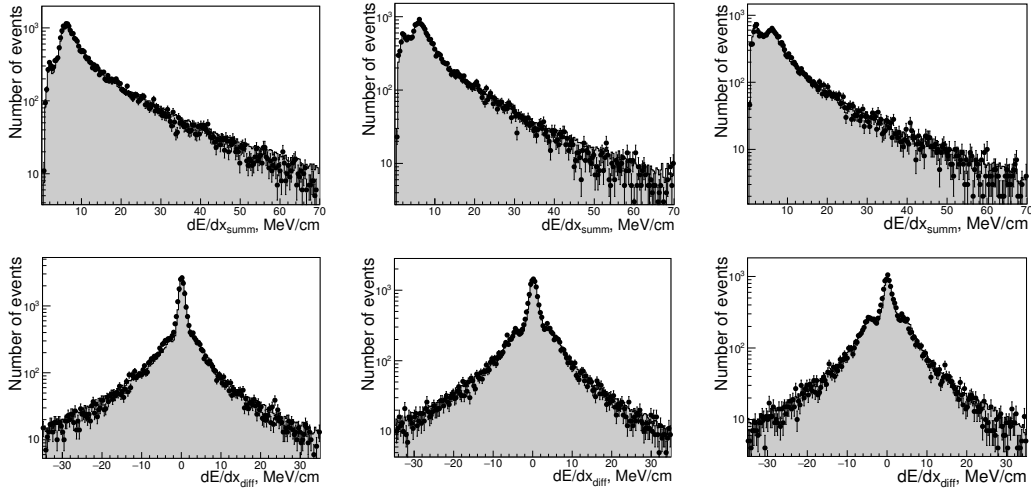


Figure 27: The dE/dx_{summ} (top figures) and dE/dx_{diff} (bottom figures) in the 1st (left), 3rd (middle) and 5th (right) double layers for the K^\pm selected from $e^+e^- \rightarrow K^+K^-\pi^+\pi^-$ events in the experiment (markers) and simulation (gray histogram). The data from all experimental runs of 2019 are used.

7. Examples of the application of the LXe-based PID

7.1. Separation of the $e^+e^-(\gamma)$ and $\pi^+\pi^-(\gamma)$ final states at $E_{\text{beam}} < 500$ MeV

The developed PID procedure can be used for the important task of the pion form factor $|F_\pi|^2$ measurement [19]. To calculate the $|F_\pi|^2$ at the given $E_{\text{c.m.}}$ point one needs to determine the number of events of the $\pi^+\pi^-(\gamma)$ final state, $N_{\pi^+\pi^-}$. The major background sources for $\pi^+\pi^-(\gamma)$ are the

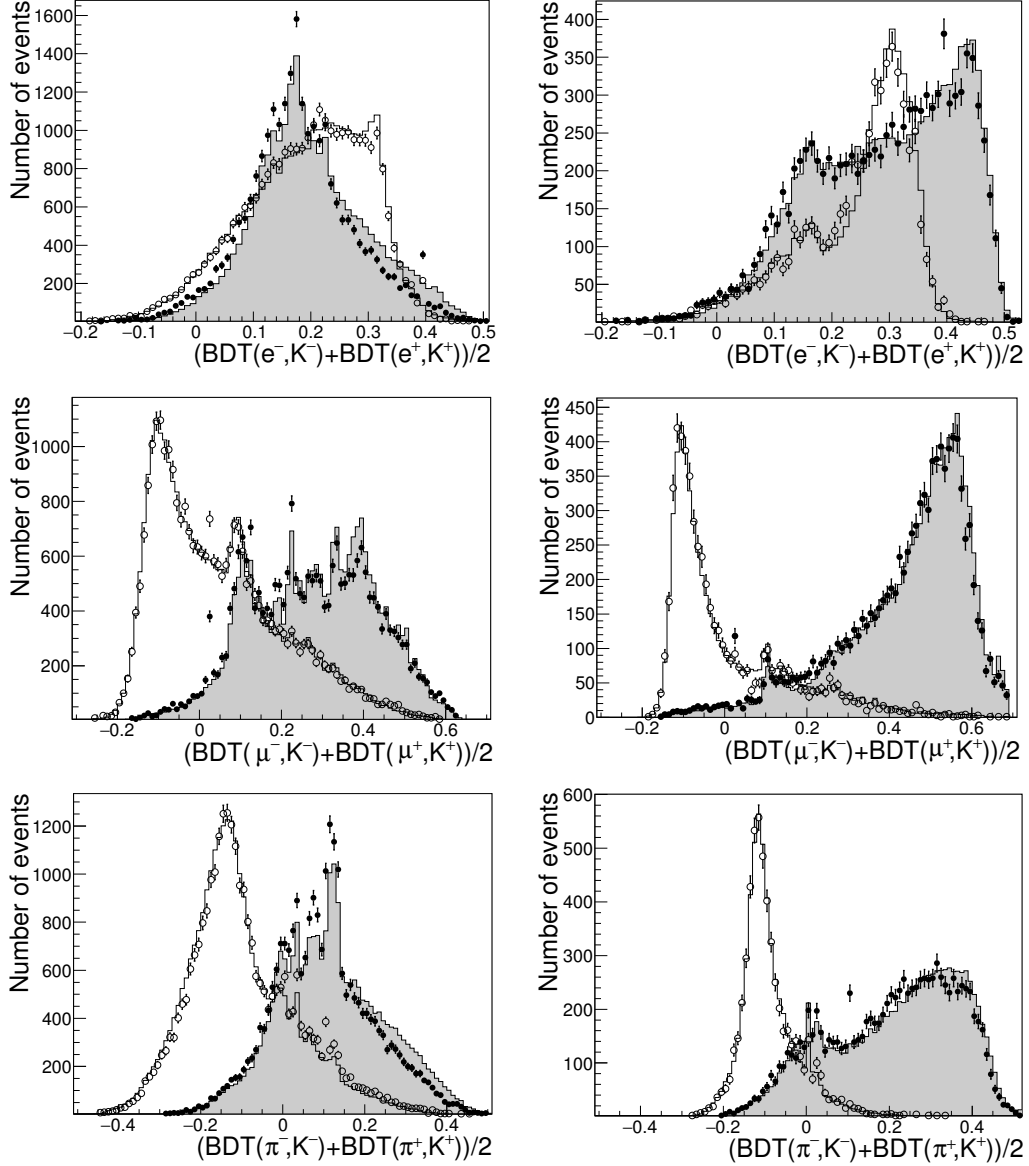


Figure 28: The $\text{BDT}(e^\pm, K^\pm)$ (top), $\text{BDT}(\mu^\pm, K^\pm)$ (middle) and $\text{BDT}(\pi^\pm, K^\pm)$ (bottom) spectra for the K^\pm and π^\pm selected from $e^+e^- \rightarrow K^+K^-\pi^+\pi^-$ events in the experiment (filled circles for K^\pm and empty circles for π^\pm) and simulation (gray histogram for K^\pm and open histogram for π^\pm). The left figures are drawn for particles with momenta lower than 400 MeV, the right – larger than 400 MeV. The data from all experimental runs of 2019 are used.

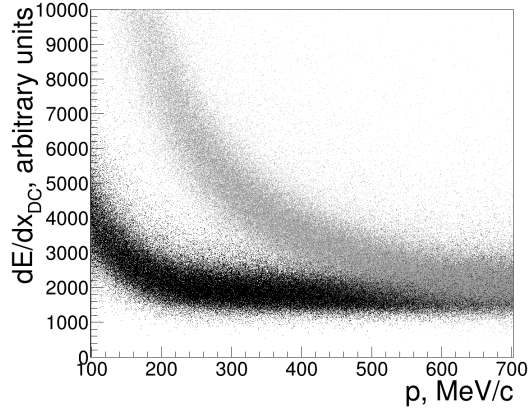


Figure 29: dE/dx_{DC} as a function of particle momentum for simulated K^\pm (gray) and π^\pm (black).

$e^+e^-(\gamma)$, $\mu^+\mu^-(\gamma)$ final states and cosmic muons. The effective separation of the $\pi^+\pi^-(\gamma)$ and $\mu^+\mu^-(\gamma)$ final states at the CMD-3 is a difficult task at the energies $E_{\text{beam}} > 350$ MeV. However, since the cross sections of the $e^+e^- \rightarrow e^+e^-(\gamma)$ and $e^+e^- \rightarrow \mu^+\mu^-(\gamma)$ processes are precisely calculated in the frame of QED, the number of events $N_{\mu^+\mu^-}$ can be calculated once the number of events $N_{e^+e^-}$ is known. In turn, determination of the $N_{e^+e^-}$ becomes possible with the application of the effective separation of the $e^+e^-(\gamma)$ and $\pi^+\pi^-(\gamma)$ final states. Currently at CMD-3 we use two independent approaches for the $e^+e^-(\gamma)$ and $\pi^+\pi^-(\gamma)$ separation: 1) using the particle momenta; 2) using the full energy depositions of particles in the calorimeter. The LXe-based PID provides us another method of $e^+e^-(\gamma)$ and $\pi^+\pi^-(\gamma)$ separation.

As an example we consider the $e^+e^-(\gamma)$ and $\pi^+\pi^-(\gamma)$ separation at the energies $E_{\text{beam}} < 500$ MeV in the experimental runs of 2018. We select events having exactly two oppositely charged tracks, satisfying the following conditions: 1) the momenta of tracks are larger than 100 MeV/c; 2) the $|\rho|$ and $|z|$ of the track point of the closest approach to the beam axis should be less than 0.6 and 12 cm, respectively; 3) the polar angles of tracks should be in the range from 1.0 to $\pi - 1.0$ rad; 4) the track collinearity conditions:

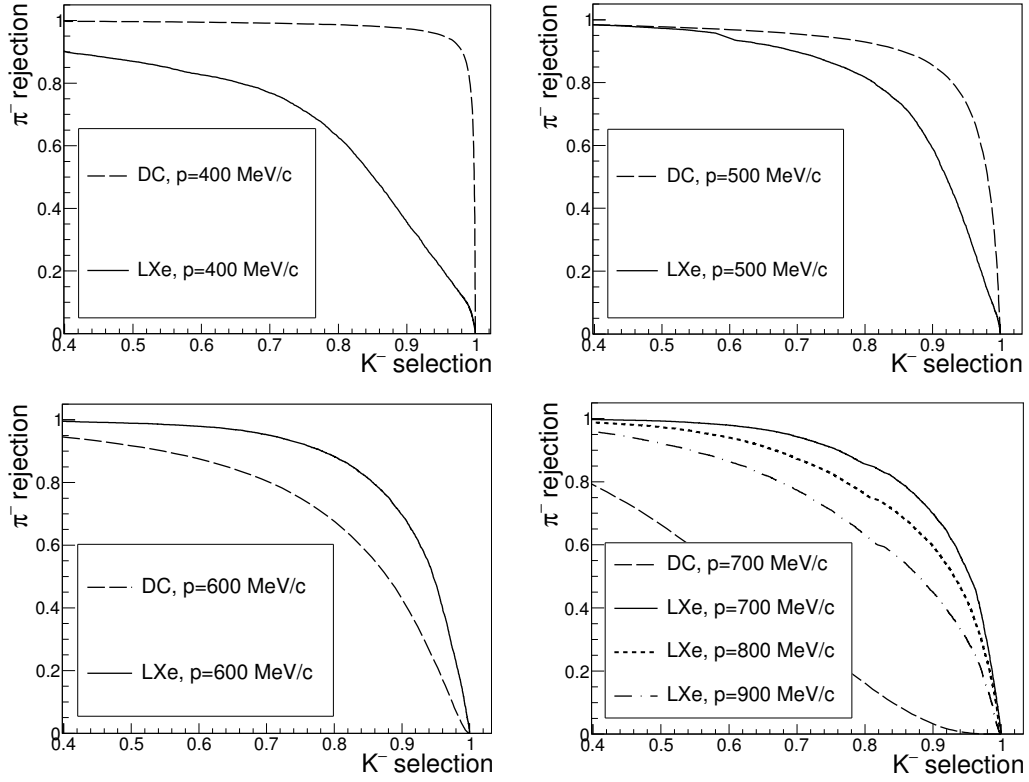


Figure 30: The ROC-curves for the BDT(π^- , K^-) classifier and dE/dx_{DC} -based π^-/K^- separation for different particle momenta according to simulation. The classifier types and particle momenta are shown in the legends.

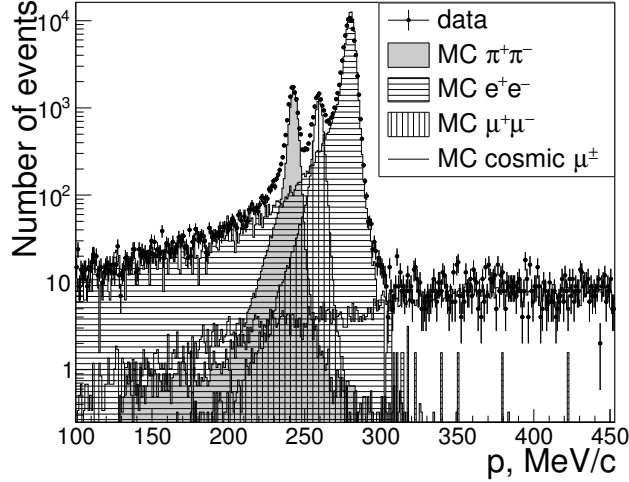


Figure 31: The momentum spectra of the particles selected at $E_{\text{beam}} = 280$ MeV in the experiment (markers), simulation of $\pi^+\pi^-(\gamma)$ (gray histogram), $e^+e^-(\gamma)$ (horizontal hatching), $\mu^+\mu^-(\gamma)$ (vertical hatching) and cosmic muons (open histogram). The black line shows the total MC of the signal and background processes.

$$|\theta_1 + \theta_2 - \pi| < 0.25 \text{ rad and } ||\varphi_1 - \varphi_2| - \pi| < 0.15 \text{ rad.}$$

Figure 31 shows the momentum spectrum for the particles, selected in the experiment and simulation at $E_{\text{beam}} = 280$ MeV. The contribution of the collinear final states is estimated according to the known cross sections of the processes and luminosity, while the contribution of the cosmic muons is estimated using the events with the momenta larger than $1.25 \cdot E_{\text{beam}}$. Further, Fig. 32 shows the distribution of the average $\text{BDT}(e, \pi)$ response for two tracks, *i.e.* $(\text{BDT}(e^-, \pi^-) + \text{BDT}(e^+, \pi^+))/2$, for $E_{\text{beam}} = 280$ MeV (left tail of the $\rho(770)$) and 380 MeV (near the peak of $\rho(770)$). It is seen that the $(\text{BDT}(e^-, \pi^-) + \text{BDT}(e^+, \pi^+))/2$ parameter provides a powerful classifier for $e^+e^-(\gamma)$ and $\pi^+\pi^-(\gamma)$ separation, see corresponding ROC-curves in Fig. 33. At $E_{\text{beam}} = 380$ MeV the classifier allows to select 99.5% of $\pi^+\pi^-(\gamma)$ events by the 98% rejection of the $e^+e^-(\gamma)$ background.

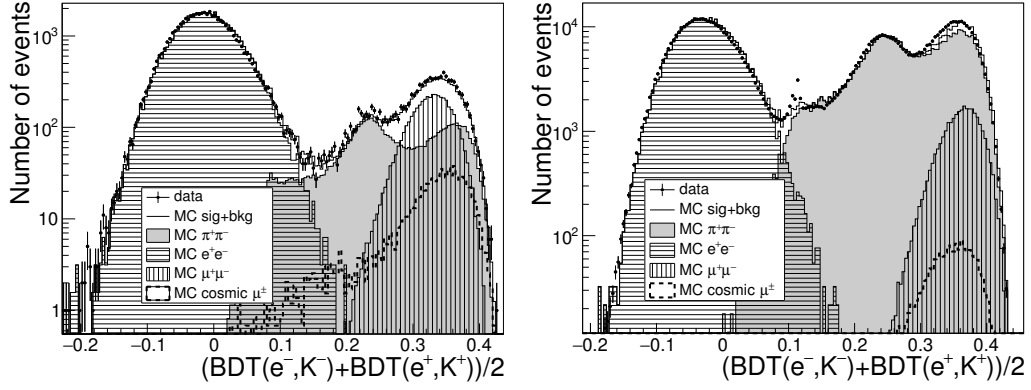


Figure 32: The distribution of the $(\text{BDT}(e^-, \pi^-) + \text{BDT}(e^+, \pi^+))/2$ (left — for $E_{\text{beam}} = 280$ MeV, right — $E_{\text{beam}} = 380$ MeV) in the experiment (markers), simulation of $\pi^+\pi^-(\gamma)$ (gray histogram), $e^+e^-(\gamma)$ (horizontal hatching), $\mu^+\mu^-(\gamma)$ (vertical hatching) and cosmic muons (dashed line). The open histogram shows the total MC of the signal and background processes.

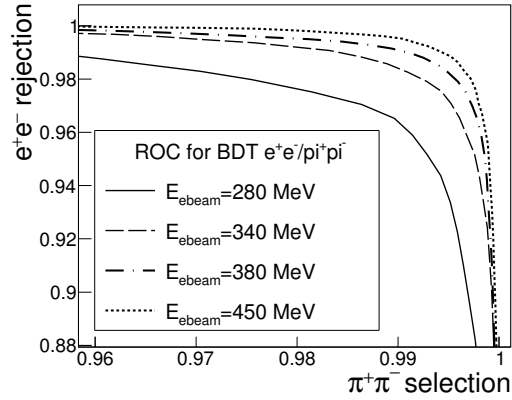


Figure 33: ROC-curves for separation of the $e^+e^-(\gamma)$ and $\pi^+\pi^-(\gamma)$ final states using $(\text{BDT}(e^-, \pi^-) + \text{BDT}(e^+, \pi^+))/2$ at different E_{beam} (see legend) according to simulation.

7.2. Selection of the K^+K^- final state at high energies

Another application of the LXe-based PID is the task of the selection of the K^+K^- final state at high energies. As an example, we perform such selection on the base of 2.2 pb^{-1} of data collected at $E_{\text{c.m.}} = 1.975 \text{ GeV}$ in the 2019 runs. To select the two-track collinear events, we apply the selections listed earlier in Section 7.1. The main background sources are the $e^+e^-(\gamma)$, $\mu^+\mu^-(\gamma)$, $\pi^+\pi^-(\gamma)$ final states and the events with cosmic muons, their contributions in simulation are estimated in a way described earlier in Section 7.1. The background suppression is done by the cuts, imposed on the values of the average BDT responses $(\text{BDT}(e^-, K^-) + \text{BDT}(e^+, K^+))/2$ and $(\text{BDT}(\mu^-, K^-) + \text{BDT}(\mu^+, K^+))/2$ for the 2 tracks, see Figs. 34–35. The cut on $(\text{BDT}(\mu^-, K^-) + \text{BDT}(\mu^+, K^+))/2$ leads to the loss of $\sim 5\%$ of signal events and also provides significant suppression of the $e^+e^- \rightarrow \pi^+\pi^-(\gamma)$ process. Since the cross section of the latter is relatively low at $E_{\text{c.m.}} \sim 2 \text{ GeV}$ and $\pi^+\pi^-$ events are kinematically separated from K^+K^- , we do not impose any cuts on $\text{BDT}(\pi^\pm, K^\pm)$.

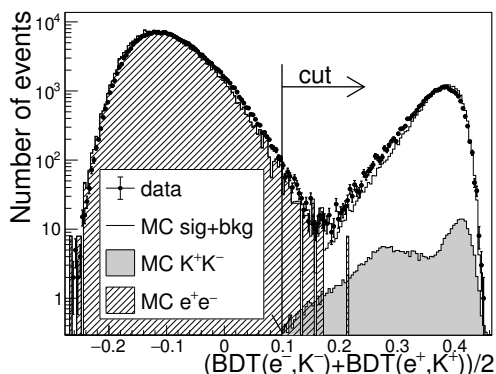


Figure 34: The $(\text{BDT}(e^-, K^-) + \text{BDT}(e^+, K^+))/2$ spectra in the experiment (markers), MC of the $K^+K^-(\gamma)$ (gray histogram), $e^+e^-(\gamma)$ (hatched histogram). The open histogram shows the total MC of the signal and background processes.

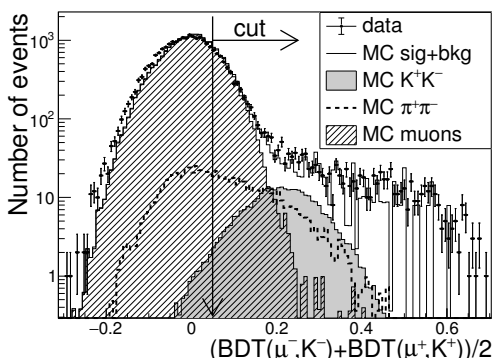


Figure 35: The $(\text{BDT}(\mu^-, K^-) + \text{BDT}(\mu^+, K^+))/2$ spectra in the experiment (markers), MC of the $K^+K^-(\gamma)$ (gray histogram), $\mu^+\mu^-(\gamma)$ and cosmic muons (hatched histogram), $\pi^+\pi^-(\gamma)$ (dotted line). The open histogram shows the total MC of the signal and background processes.

Next, the signal/background separation is performed by approximation of the distribution of “energy disbalance” ΔE , defined as

$$\Delta E = \frac{\sqrt{\vec{p}_+^2 c^2 + m_{K^+}^2 c^4} + \sqrt{\vec{p}_-^2 c^2 + m_{K^-}^2 c^4} + |\vec{p}_+ + \vec{p}_-| c}{2E_{\text{beam}}} - 1, \quad (6)$$

where \vec{p}_\pm are the particle momenta. The additional term $|\vec{p}_+ + \vec{p}_-|$, corresponding to the total momentum of two tracks, allows to get rid of the superimposition of the signal peak with the $e^+e^-(\gamma)$ radiative tail. Figure 36 shows the ΔE spectra before and after the application of cuts on BDT. It is seen that after the background suppression the signal/background separation in the ΔE spectrum becomes possible. To perform the separation, we approximate the experimental ΔE spectra using the sum of three Gaussians to approximate the peaking background and the linear function to approximate the contribution of cosmic muons. The shape of the signal peak is fixed from the approximation of the simulated ΔE spectra for the $e^+e^- \rightarrow K^+K^-$ process, except for the shift of the signal peak as a whole and its additional broadening, which are added as the floating parameters. Thus, we obtain 548 ± 27 of signal events at $E_{\text{c.m.}} = 1.975$ GeV (Fig. 36, right).

It should be noted that for the c.m. energies larger than 1.5 GeV usage of the LXe-based PID is the only way to measure the $e^+e^- \rightarrow K^+K^-$ process cross section at CMD-3.

8. Conclusions

The procedure of the charged PID using the LXe calorimeter of the CMD-3 detector was developed. The procedure uses the energy depositions, measured in 12 layers of the LXe calorimeter, as the input for the set of boosted decision trees classifiers, trained for the separation of the electrons, muons, pions and kaons in the momentum range from 100 to 1200 MeV/c. Since the event samples for the classifier training are taken from the MC, special attention was paid to the tuning of the simulated detector response.

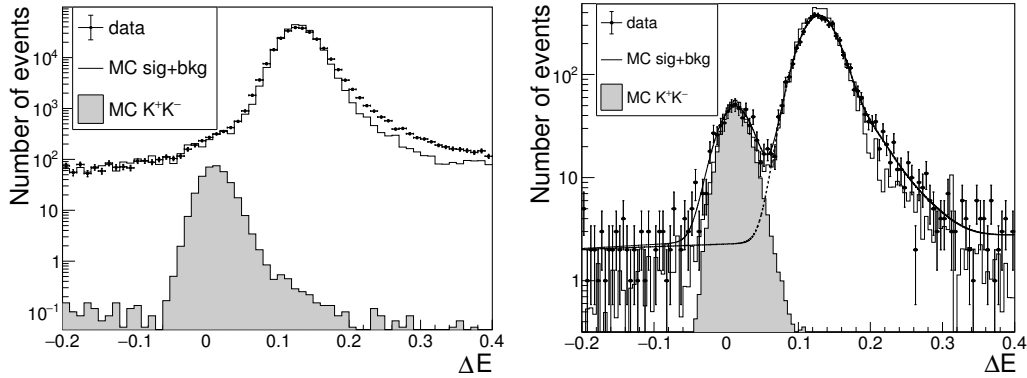


Figure 36: The ΔE spectra before (left) and after (right) background suppression in the experiment (markers) and MC of the $K^+K^-(\gamma)$ (gray histogram). The open histogram shows the total MC of the signal and background processes. The solid curve on the right picture shows the fit of the distribution in the experiment, dotted curve — the background part of the fit.

From the experimental side the procedure of the calibration of strip channels of LXe calorimeter with the precision of about 1% was developed. These efforts resulted in good data/MC agreement for the classifier responses for all particle types. Finally, the application of the method was demonstrated by the examples of separation of the $e^+e^-(\gamma)$ and $\pi^+\pi^-(\gamma)$ final states at $E_{\text{beam}} < 500$ MeV and of the selection of the K^+K^- final state at high energies.

9. Acknowledgments

We thank the VEPP-2000 personnel for excellent machine operation. Part of work related to the method of the selection of $e^+e^- \rightarrow K^+K^-\pi^+\pi^-$ process events mentioned in the Section 6.4 is partially supported by the grant of the Russian Foundation for Basic Research 20-02-00496 A 2020.

REFERENCES

- [1] V.V. Danilov et al., Proceedings EPAC96, Barcelona, p.1593 (1996).
- [2] I.A. Koop, Nucl. Phys. B (Proc. Suppl.) 181-182, 371 (2008).

- [3] P.Yu. Shatunov et al., Phys. Part. Nucl. Lett. 13, 995 (2016).
- [4] D. Shwartz et al., PoS ICHEP2016, 054 (2016).
- [5] B.I. Khazin et al. (CMD-3 Collaboration), Nucl. Phys. B (Proc. Suppl.) 181-182, 376 (2008).
- [6] F. Jegerlehner, Springer Tracks Mod. Phys. 274, 1 (2017).
- [7] M. Davier, A. Hoecker, B. Malaescu, and Z. Zhang, Eur. Phys. J. C 77, 827 (2017).
- [8] A. Keshavarzi, D. Nomura, T. Teubner, Phys. Rev. D 97, 114025 (2018).
- [9] K. Hagiwara et al., J. Phys. G 38, 085003 (2011).
- [10] D. Epifanov (CMD-3 Collaboration), J. Phys. Conf. Ser. 293, 012009 (2011).
- [11] A. Amirkhanov et al., Nucl. Instrum. Meth. A936, 598 (2019).
- [12] F. Grancagnolo et al., Nucl. Instr. Meth. A623, 114 (2010).
- [13] A.V. Anisyonkov et al., Nucl. Instr. Meth. A598, 266 (2009).
- [14] V.E. Shebalin et al., JINST 9 (10), C10013 (2014).
- [15] H. Voss, A. Hcker, J. Stelzer, F. Tegenfeldt, PoS(ACAT) 040.
- [16] K.I. Kakhuta and Yu.V. Yudin, Nucl. Instr. and Meth. A **598**, 342 (2009).
- [17] D.N. Shemyakin et al. (CMD-3 Collaboration), Phys.Lett. B 756, 153 (2016).
- [18] R.R. Akhmetshin et al. (CMD-3 Collaboration), Phys. Lett. B 794, 64 (2019).
- [19] F.V. Ignatov et al. (CMD-3 Collaboration), EPJ Web Conf. **218**, 02006 (2019).